



HAL
open science

SiO Evaporated Films Topography and Nematic Liquid Crystal Orientation

M. Monkade, Ph. Martinot-Lagarde, Geoffroy Durand, C. Granjean

► **To cite this version:**

M. Monkade, Ph. Martinot-Lagarde, Geoffroy Durand, C. Granjean. SiO Evaporated Films Topography and Nematic Liquid Crystal Orientation. *Journal de Physique II*, 1997, 7 (11), pp.1577-1596. 10.1051/jp2:1997204 . jpa-00248537

HAL Id: jpa-00248537

<https://hal.science/jpa-00248537>

Submitted on 4 Feb 2008

HAL is a multi-disciplinary open access archive for the deposit and dissemination of scientific research documents, whether they are published or not. The documents may come from teaching and research institutions in France or abroad, or from public or private research centers.

L'archive ouverte pluridisciplinaire **HAL**, est destinée au dépôt et à la diffusion de documents scientifiques de niveau recherche, publiés ou non, émanant des établissements d'enseignement et de recherche français ou étrangers, des laboratoires publics ou privés.

SiO Evaporated Films Topography and Nematic Liquid Crystal Orientation

M. Monkade (^{1,*}), Ph. Martinot-Lagarde (^{1,**}), G. Durand (¹) and C. Granjean (²)

(¹) Laboratoire de Physique des Solides (**), Bâtiment 510, Université Paris-Sud,
91405 Orsay Cedex, France

(²) Laboratoire de Génétique Moléculaire, Bâtiment 32, CNRS,
91198 Gif-sur-Yvette Cedex, France

(Received 24 October 1996, revised 1 July 1997, accepted 29 July 1997)

PACS.61.30.Eb – Experimental determinations of smectic, nematic, cholesteric and other structures

PACS.61.16.-d – Electron, ion, and scanning probe microscopy

PACS.68.55.Jk – Structure and morphology; thickness

Abstract. — We present transmission electron microscopy micrographs of SiO films obliquely evaporated on indium-tin oxide coated glass surfaces. To study the growth mechanism of these SiO films, we present film cross sections in the evaporation plane. Varying the evaporation angle, we observe a column to needle transition, with increasing surface roughness. This transition corresponds to the planar to oblique nematic liquid crystal orientation transition, through the bistable one. The SiO surface roughness is estimated to induce a nematic surface order decrease (surface melting). The azimuthal nematic orientation on these plates corresponds to the direction of minimum surface melting. This confirms the predictions of the Barbero-Durand model.

1. Introduction

Nematic liquid crystals are oriented liquids. Their molecules tend to orient parallel to each other along one direction characterized by the director \mathbf{n} ($\mathbf{n}^2 = 1$). This direction is arbitrary in space and imposed by the anisotropic interactions between nematic liquid crystal molecules and a boundary wall [1]. These surface-bulk anisotropic interactions have extensively been studied for two reasons: first, an academic one, is the understanding of the mechanism by which an homogeneous orientation of the nematic molecules is imposed on a substrate; second, a more practical one, is the control of these orientations. Uniform and homogeneous orientation of the nematic liquid crystal was obtained by using various surface treatments including mechanical striations or rubbing of thin polymeric layers [2]. Deposition of SiO by evaporation at oblique incidence has been long ago known to provide nematic liquid crystal alignment [3]. Later it was shown that SiO layers can give rise to two different kinds of homogeneous, strong and stable

(*) *Permanent address:* Laboratoire Matière Condensée, Département de Physique, Faculté des Sciences d'El Jadida, Université Chouab Doukkali, El Jadida, Maroc.

(**) Author for correspondence (e-mail: martinot@lps.u-psud.fr)

(***) URA 2 CNRS

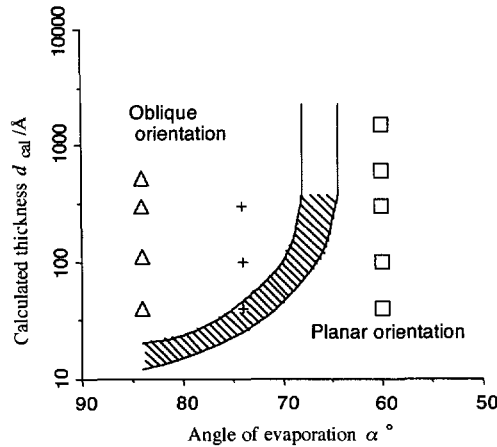


Fig. 1. — (α, d) Phase diagram for the nematic 5CB surface orientation *versus* the evaporation angle α and the layer thickness calculated from the quartz balance measurements: d_{cal} . The dashed area is the transition region where a two times degenerate oblique orientation allows a continuous transition between the planar orientation (lower right) and non degenerate oblique orientation (upper left). The marks (Δ , +, \square) show the points used in our electron microscopy investigations.

alignment of nematic liquid crystal molecules, depending on the evaporation conditions [4, 5]. For an angle of evaporation incidence $45^\circ < \alpha < 80^\circ$, from the normal of the substrate, the nematic liquid crystal orientation is planar with molecules lying above the solid surface along a direction perpendicular to the incidence plane. For grazing incidence $80^\circ < \alpha < 90^\circ$, the nematic liquid crystal orientation is oblique in the incidence plane with a tilt angle toward the evaporation direction. The topography of these SiO obliquely deposited films has been studied by different techniques of electron microscopy [6–13]. It shows an anisotropic structure of *columns* or *needles* related to anisotropic nucleation and growth on the substrate. The available evidence from these electron microscope studies has not been sufficient to completely characterize the columnar structure. In most experiments the *columns* are seen from above and their geometrical parameters are not clearly measured. A cross section was only shown in reference [9]. The growth and the roughness of the SiO layer are rarely shown. The orientation properties of nematic liquid crystal molecules on the surface were explained by elastic models: the nematic is deformed to minimize its elastic energy in response to the anisotropic structure of SiO obliquely evaporated films [4, 10]. For the planar orientation the nematic liquid crystal molecules would align parallel to some assumed SiO surface undulations perpendicular to the evaporation plane. For the oblique orientation the nematic liquid crystal molecules were supposed to align parallel to SiO oblique *needles* or *columns*.

More recently, the orientation of nematics on a glass substrate SiO evaporated at oblique incidence have been studied in more details [14]. It was shown that the surface orientation of nematic liquid crystal molecules varies with the evaporation angle α and the thickness of the SiO layer d . A nematic orientation phase diagram (α, d) was presented for 5CB (pentyl cyanobiphenyl). This diagram (Fig. 1) shows a continuous transition between the planar and the oblique orientations. In this transition region the nematic liquid crystal orientation rotates on the surface. In the oblique region, the nematic tilt angle increases with d and saturates. The orientation transition, the rotation of the orientation in the transition region and the saturation of oblique orientation cannot be explained by the elastic models. We can hardly imagine a rotation of *needles* or *columns*. The results were quantitatively explained by an “order electric”

model. In this model, the SiO roughness destroys the nematic order at the surface, inducing a gradient of this nematic order toward the ordered bulk [15]. An order electric polarization proportional to this gradient of nematic order gives rise to an electrostatic term in the nematic orienting surface free energy. This allows to describe the planar and oblique orientations and the rotation of nematic liquid crystal molecules in the transition region. Such a decrease of nematic order on those SiO obliquely deposited films has been observed by Barberi *et al.* [16]. To check the order electric model, it is then important to characterize the surface roughness of SiO evaporated films *versus* α and d .

In this paper, we observe the topography and we estimate the roughness of SiO obliquely deposited films on ITO coated glass substrates. We try to establish a correlation between this topography and the nematic liquid crystal molecules orientation presented in the phase diagram (α, d). To observe the surface topography, we use a combination of two transmission electron microscopy techniques: the surface shadowing technique and the ultramicrotomy one. In Section 2 we present the experimental methods. We then show, in Section 3, series of micrographs and measurements of the surface parameters. We compare our results with literature data in Section 4. Finally in Section 5 we discuss the effect of the surface topography and roughness on the nematic liquid crystal molecules orientation on the same SiO obliquely evaporated films used in our electron microscopy investigations.

2. Experimental Methods

Electron Microscopy (EM) is one of the most direct techniques for obtaining information from surface topography and roughness. For high resolution, the Transmission Electron Microscopy (TEM) is a powerful technique but special specimen preparation techniques are usually needed [17]. Generally, the TEM of SiO obliquely evaporated films has been investigated using appropriate electron microscopy thin substrates like amorphous carbon films, however the nematic liquid crystal molecules orientation is determined not on the amorphous carbon films but on glass substrates prepared under similar conditions. One can suspect possible differences between the topography and the roughness of the SiO layer deposited on electron microscopy substrate and on the glass. To avoid any doubt about this matter, our EM investigations were made on the same ITO glass plates used to observe the nematic orientation phase diagram and the measurement of the nematic liquid crystal orientations. This choice implies to overcome different technical difficulties. We must obviously get rid of the glass substrate to keep only the thin SiO evaporated film for the electron microscope observations. We begin first with a platinum shadowing evaporation on the SiO obliquely deposited ITO glass plate; then, we deposit a carbon layer on the platinum. We finally separate the glass plate from the platinum-carbon-SiO film by dissolving the ITO in an acid solution. We finally observe the platinum-carbon-SiO film directly or after ultramicrotomy to prepare oriented cross sections.

2.1. SiO-ITO GLASS PLATES PREPARATION. — The ITO coated Baltracon glass plate from Balzers is placed in an evaporator under vacuum ($\sim 10^{-5}$ T) at an oblique angle (Fig. 2). The silicon oxide SiO vapor is obtained by heating the SiO in a crucible at high temperature. A quartz is placed normally to the evaporation direction. The evaporated mean normal thickness d_{qz} of the deposited SiO film is measured from the frequency shift of the oscillating quartz. Knowing the incidence angle α of the SiO on the glass (Fig 2), we calculate the mean evaporation thickness d_{cal} on the glass by: $d_{cal} = d_{qz} \cos \alpha$. This calculated SiO thickness d_{cal} on the glass is varied from 40 Å to 1500 Å. We have used three different values of the evaporation angle α . The first one $\alpha = 84^\circ$ gives rise to an oblique orientation of the nematic. The second $\alpha = 60^\circ$ corresponds to a planar alignment and an intermediate value $\alpha = 74^\circ$

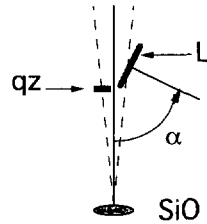


Fig. 2. — Deposition of SiO by evaporation at oblique incidence α on the ITO coated Baltracon glass plate L . The mean SiO film thickness is measured by frequency shift of the oscillating quartz (qz) then corrected with respect to the angle of incidence.

which could lead to intermediate nematic orientation. For each angle α , we prepare at the same time three plates, one for the electron microscopy observations and the two others for the nematic liquid crystal orientation test.

2.2. ELECTRON MICROSCOPY SAMPLE PREPARATION

2.2.1. Platinum-Carbon Deposition Conditions. — The SiO-ITO glass plate is placed in a platinum carbon evaporator. The platinum is evaporated at an oblique angle of 70° from the normal plate in the SiO evaporation plane. A carbon layer (of thickness 100 \AA to 200 \AA) is further deposited onto the surface at normal incidence. This thin carbon layer does not contribute appreciably to the final electron microscope image

2.2.2. Separation of the Carbon-Platinum - SiO Films from the Glass Plate. — After the platinum-carbon deposition the sample is introduced in an acid solution (50% H_2O , 47% HCL and 3% HNO_3) which dissolves ITO [8]. After a few seconds, the platinum SiO film, strengthened by the carbon layer, separates from the thick glass plate after the ITO dissolution. The film, floating on the solution surface, is picked up on a marked electron microscope grid G1 (Fig. 3, b1) and washed with distilled water prior to the transmission electron microscope observations. At this stage, the evaporation orientation is lost.

2.2.3. Transmission Electron Microscopy Observations. — The TE microscope used is a Philips 300 which is operated at an electron beam accelerating potential of 60 to 80 KV. To find back the lost evaporation direction we compare the electron microscope image with the image obtained on an other SiO film. This film is evaporated under the same conditions on a thin carbon film supported by a marked EM grid G2 (Fig. 3, a1). The mark on the grid G2 indicates the evaporation plane direction e . The corresponding microscopic image (sketched in a2) shows objects pointing in the same direction e . On the image b2 of grid G1, one finds back the same objects with an arbitrary rotation. The comparison of the two pictures a2 and b2 gives the evaporation plane direction e on the grid G1.

2.2.4. Ultramicrotomy. — The sample on the grid G1 is oriented to have the SiO evaporation plane direction e in the section plane of the ultramicrotome and is embedded in a low viscosity epoxy with low polymerization temperature [18]. Practically to keep the film orientation, the sample is placed on a first solid epoxy layer and covered by a fluid second one. The specimen becomes solid after a few hours. It is then placed in an ultramicrotome (L.K.B.) and trimmed to a sectioning face with a glass knife. When close to the sample, the glass knife is replaced by a diamond knife horizontally and vertically adjusted. One obtains sample thin sections which are collected on a distilled water solution with a surface tension sufficiently high to permit

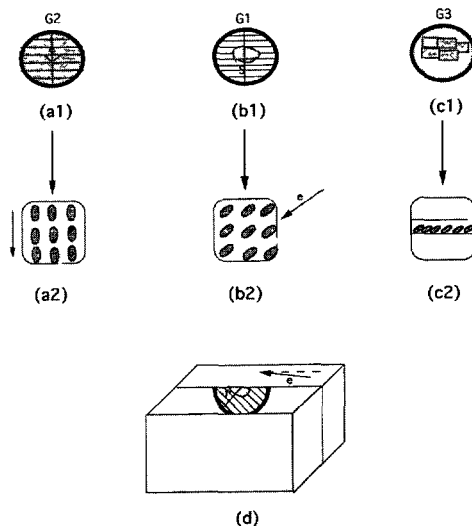


Fig. 3. — Identification of the evaporation direction e for the ultramicrotomy section. G1, G2, G3 are the electron microscope grids: a1 shows the evaporated SiO film on the marked grid G2. b1 shows the sample S picked up on the grid G1 after the ITO dissolution. c1 shows the ultramicrotomy cross sections of the SiO film on the grid G3. a2, b2 and c2 are the electron microscope images of a1, b1 and c2. d shows the sample included in the epoxy during the ultramicrotomy section: The grid G1 is oriented so that the evaporation plane is in the section plane.

optimum wetting of the diamond knife edge and to keep the sections afloat. The thin sections, observed from their Newton colors (grey) are picked up on an EM grid G3 (Fig. 3, c1) rinsed and dried. A thin carbon film is then normally evaporated onto this grid to fix the sections prior to the observations in the TEM.

2.3. NEMATIC LIQUID CRYSTAL ORIENTATION TEST. — The nematic mean molecular orientation on the SiO obliquely evaporated glass plate is optically determined. A wedged nematic sample of 5CB (pentyl-cyanobiphenyl) is made by using the two previous plates facing each other (Fig. 4). The plate evaporation directions are placed antisymmetrically. For oblique surface orientation, this is expected to result in uniformly tilted samples. The wedge produced by a $50 \mu\text{m}$ wire spacer at 1 cm distance, allows the observation of birefringence fringes under a polarized microscope. From the fringe spacing and the knowledge of the refractive indices of the material [19], we can deduce $\cos^2 \theta$; θ is the molecular tilt angle with respect to the normal of the plate. The accuracy of the $\cos^2 \theta$ determination is ± 0.05 . The azimuthal angle φ , compared to the evaporation plane, is deduced from the observation of the optical sample neutral lines, *i.e.* from the orientation of the crossed polarizer and analyzer for maximum extinction.

3. Results

We present our results in a series of micrographs taken at the same magnification for three different values of the evaporation zenithal angle α . For each value of α , we present micrographs for different SiO calculated thicknesses d_{cal} . At each thickness d_{cal} , we show a pair of micrographs. The first is a counter-type TEM micrograph of the SiO film surface seen from above. The second is an usual TEM micrograph of the ultramicrotomy section of the same film

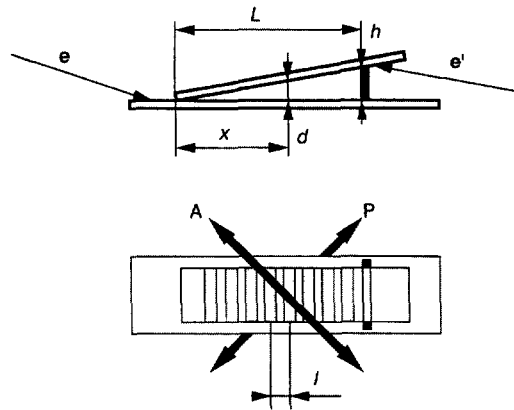


Fig. 4. — Wedged nematic sample made between two ITO glass plates with antisymmetrically evaporation direction (e , e'). The surface orientation of nematic molecules is deduced from the birefringence fringes spacing l observed under a polarized microscope. P is the polarizer, A is the analyser.

viewed from the side. The two micrographs are complementary and give a complete description of the topography and the roughness of the SiO film. The comparison of these micrographs at the same evaporated zenithal angle α or at the same thickness d_{cal} shows the influence of the two evaporation parameters on the topography and the roughness.

3.1. GRAZING INCIDENCE: $\alpha = 84^\circ$. — The series of micrographs of Figure 5 shows the appearance of evaporated SiO films for increasing thickness, seen from above (O1a, O2a, O3a, O4a) and their ultramicrotomy sections which give a side view (O1s, O2s, O3s, O4s). On the sections, grey tilted SiO objects are visible. The small black grains (20–40 Å) on their tops and sometimes in their sides are the platinum deposition. On the view from above (counter type), the platinum decorates in white the objects. In the literature, these objects are named *columns* or *needles*. For this grazing incidence, we prefer to name these objects *needles* because their individual diameter varies.

The *needles* point in the evaporation plane at an angle a from the plate normal toward the evaporation source. For thin thickness $d_{\text{cal}} = 40$ Å, their tilt a is 35° as shown on micrograph O1s. For thicker films $d_{\text{cal}} = 110$ Å (O2s), $d_{\text{cal}} = 300$ Å (O3s) and $d_{\text{cal}} = 520$ Å (O4s), the tilt angle is 40° to 45° . On O3s, one can see at the beginning of the film some *needles* which have grown at 35° tilt. It is plausible to think that the initial tilt of 35° is influenced by the ITO substrate; when the *needles* get thicker, their tilt (40° – 45°) would become independent of the substrate and would be defined by the evaporation parameters. Note however that the thin cross sections seem to be distorted by the cut, which leads to a relatively large uncertainty.

We measure the average altitude of the needle tops d_{mes} on the cross sections. It is larger than the thickness calculated from the quartz measurements: d_{cal} . We have plotted the variation of d_{mes} versus d_{cal} in Figure 6. The slope of the log-log plot is 0.77 which indicates the beginning of a saturation. Nevertheless the continuous growth of d_{mes} is well above the linear dependence $d_{\text{mes}} = d_{\text{cal}}$, indicated by the straight line. These two thicknesses should be equal for a compact SiO layer. The difference between d_{mes} and d_{cal} is the indication of a porous layer. The *needles* length $l = d_{\text{mes}} / \cos a$ and their diameter b , measured also on the cross sections, increases with d_{cal} . Their spacing (Fig. 7) can be measured on the view from above and on the cross sections. The results of these measurements are shown in Table Ia. The *needles* spacing,

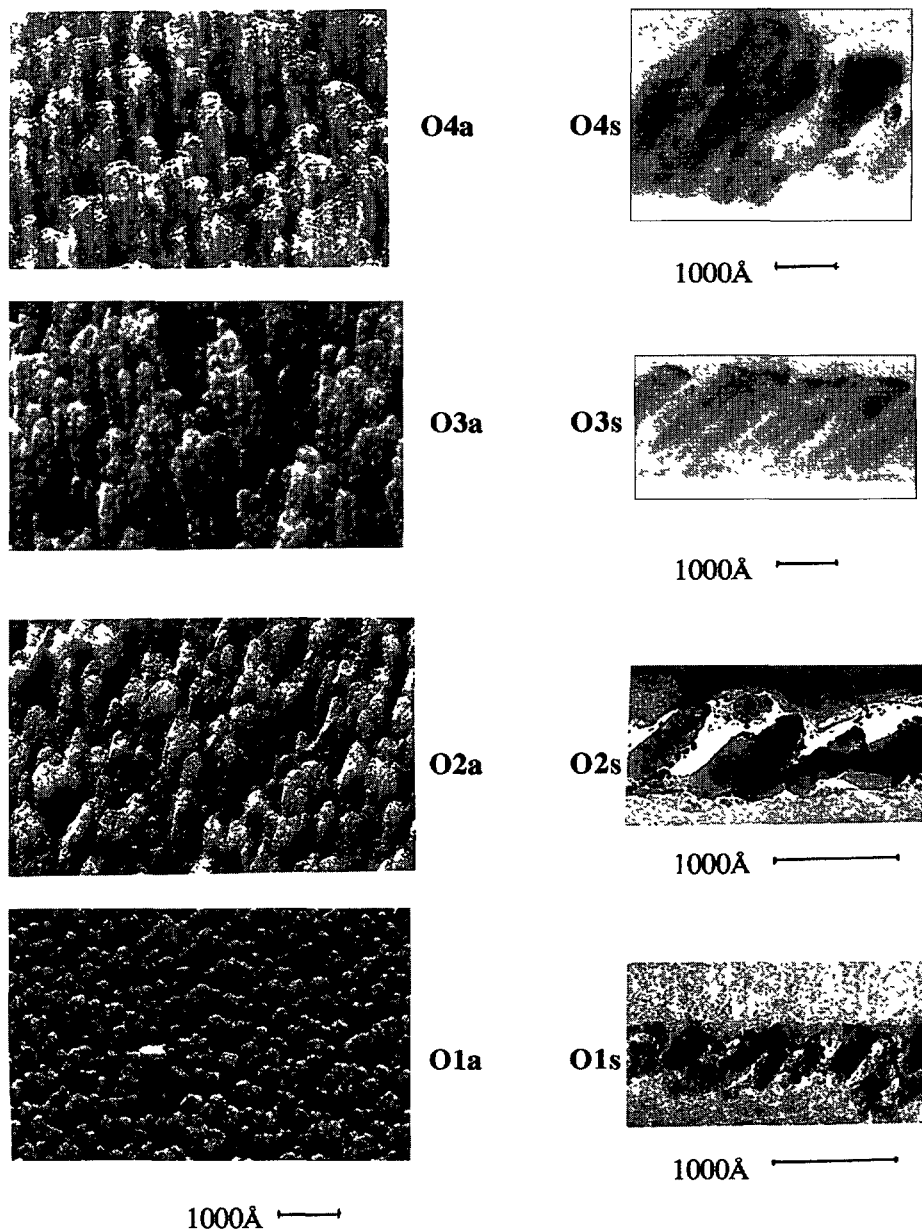


Fig. 5. — Micrographs of SiO films deposited at grazing incidence $\alpha = 84^\circ$ for different thicknesses (O1 : $d_{\text{cal}} = 40 \text{ \AA}$; O2 : $d_{\text{cal}} = 110 \text{ \AA}$; O3 : $d_{\text{cal}} = 300 \text{ \AA}$; O4 : $d_{\text{cal}} = 520 \text{ \AA}$). The SiO film structure is seen from above in the left of the figure where the SiO *needles* appear in white (counter-type). In the right of the figure, the same structure is seen from the side; here the *needles* appear in black (usual micrograph). The structure is very rough and porous.

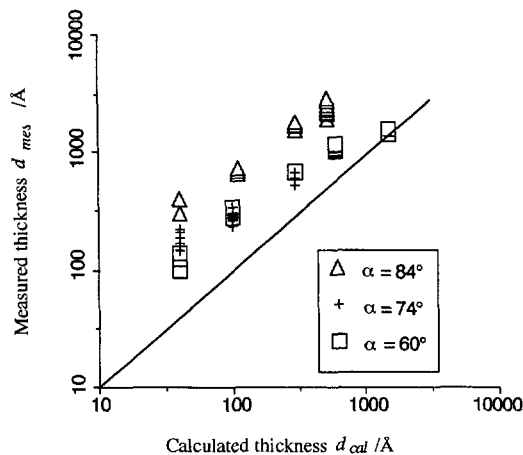


Fig. 6. — The thickness d_{mes} (measured in \AA on the film section) versus d_{cal} (calculated in \AA from the quartz balance measurement) for the three angles of incidence. a): $\alpha = 84^\circ$; b): $\alpha = 60^\circ$; c): $\alpha = 74^\circ$. For $\alpha = 84^\circ$, the curve shows a continuous growth above the linear dependence $d_{mes} = d_{cal}$ shown by the straight line. For $\alpha = 60^\circ$, d_{mes} tends to d_{cal} when the film thickness increases. One point on the diagram is the averaged thickness measured on thirty points on one sample. The dimension of the markers gives the error ($\pm 15\%$). We can see that the difference between the different samples is in the same order of magnitude as the dispersion on one simple.

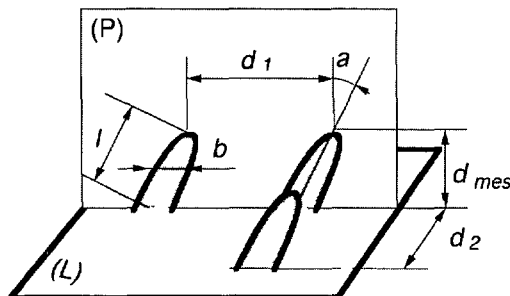


Fig. 7. — Geometric surface parameters of an obliquely evaporated SiO film. d_{mes} is the film thickness. The columns or needles are characterized by their tilt angle a , their length l , their mean diameter b , their spacing d_1 in the evaporation plane P and their spacing d_2 in the perpendicular direction.

in the range of a few hundred \AA , is larger in the evaporation plane (d_1) than in the perpendicular direction (d_2).

Let us characterize the “porosity” of this SiO film. When we measured the column diameter b , we made a thickness average: it is now reasonable to visualize the needles as tilted cylinders of constant diameter b . These cylinders are spaced by d_1 and d_2 (Fig. 7). We call x the relative area occupied by the needles. One has obviously:

$$x = \pi(b^2/4)/d_1d_2. \quad (1)$$

Locally, the relative area $1 - x$ is then void. On the other hand, the equality of the SiO volume on the plates and on the quartz surface gives:

$$d_{cal} = \bar{x} d_{mes} \quad (2)$$

Table I. — Geometrical parameters of SiO layers with different thicknesses. The layers are evaporated following an angle of 84° and they give an oblique nematic liquid crystal orientation. d_{cal} is the mean layer thickness, d_{mes} is the thickness measured at the top of the layer, l is the length of the needles and b their diameter. The distances between the needles measured along the evaporation plane and perpendicular to it are respectively d_1 and d_2 . x and \underline{x} are the relative area occupied by the needles on the plate. x is calculated with the needles measured parameters and \underline{x} is calculated from the evaporated SiO volume.

a)

| Plate | $d_{\text{cal}}/\text{\AA}$ | $d_{\text{mes}}/\text{\AA}$ | $l/\text{\AA}$ | $b/\text{\AA}$ | $d_1/\text{\AA}$ | $d_2/\text{\AA}$ | a |
|-------|-----------------------------|-----------------------------|----------------|----------------|------------------|------------------|------------|
| O1 | 40 | 330 | 430 | 110 | 350 | 230 | 35° |
| O2 | 110 | 710 | 930 | 150 | 650 | 200 | 45° |
| O3 | 300 | 1370 | 2450 | 220 | 810 | 300 | 45° |
| O4 | 520 | 2370 | 3100 | 260 | 800 | 300 | 40° |

b)

| Plate | x | \underline{x} |
|-------|------|-----------------|
| O1 | 0.12 | 0.12 |
| O2 | 0.14 | 0.15 |
| O3 | 0.16 | 0.21 |
| O4 | 0.22 | 0.22 |

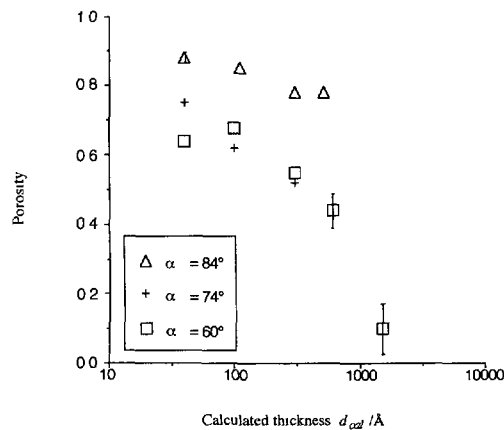


Fig. 8. — Variation of the SiO film porosity defined as the ratio $1 - d_{\text{cal}}/d_{\text{mes}}$ versus the calculated quartz thickness d_{cal} in \AA , for the three values of the evaporation angle α .

Using the data of Table Ia, we calculate x and \underline{x} as presented in Table Ib. Within our present accuracy, these two values are equal. This induce us to think that the needles are compact. For now on, we keep the definition (2) for the filling factor $x = \underline{x}$. The porosity can be simply characterized by the relative void area $1 - x = 1 - d_{\text{cal}}/d_{\text{mes}}$. The variation of this porosity parameters $1 - x$ versus d_{cal} is plotted in Figure 8. The graph shows that the porosity decreases with d_{cal} with a tendency to saturation. This saturation would mean that, for very thick layers,

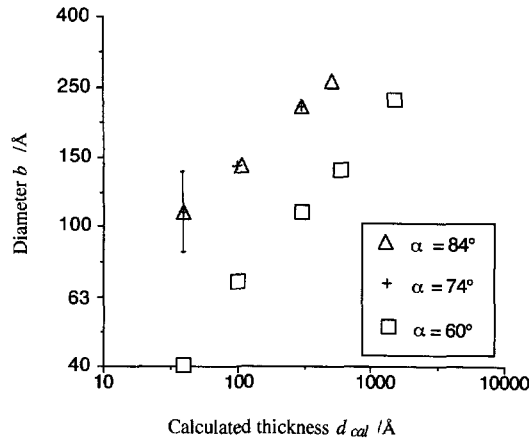


Fig. 9. — Dependence of the *columns* averaged diameter b in Å versus d_{cal} in Å for the three values of the evaporation angles α ; b grows very slowly with d_{cal} .

the *columns* grow mainly in length. We have also plotted the variation of the averaged diameter b of the *needles* versus d_{cal} in Figure 9. The graph shows that b grows very slowly and tends to saturate (on the log-log plot the slope is 0.34). The initial decrease of the porosity $1 - x$ (Fig. 8) and its saturation for larger thicknesses corresponds to the cubic root variation of the *needles* diameter b .

The measured values of the spacing d_1 and d_2 between the *needles* listed in Table Ia show that d_1 increases significantly with d_{cal} although d_2 is almost constant. The factor two jump of d_1 between $d_{cal} = 40$ Å and $d_{cal} = 520$ Å indicates a period doubling of *needles* in the evaporation plane. On the average, for thick layers, two *needles* merge to give only one that continues to grow.

As we can see the *needles* spacing and the large porosity give a very rough aspect to the SiO layer deposited at this grazing incidence. To define quantitatively the SiO surface roughness, one should make an harmonic analysis of the *needles* profile shown on the cross sections O1s, O2s, O3s, O4s. This is out of the scope of the present work. We can simply note that the largest wave length modes correspond to the spatial periods d_1 and d_2 with amplitudes larger than the periods, since one can observe deep holes between *needles*. We also observe (micrographs Oa) on the *needles* lateral surface large irregularities at spatial periods $\lambda \sim 200$ Å, 100 Å, with amplitudes comparable with the periods. On the *needles* surface a roughness of wave length $\lambda \sim 20$ Å to 40 Å is visible. This roughness appears also on all the other top view micrographs. It seems to us that it is an artifact due to separated platinum grains. In Figure 5-O3s for example we can see on the top of the *needles* that the grains joint together and create a film without any roughness of wave length 40 Å. If there is any roughness of this wave length its amplitude is very small.

3.2. LOWER INCIDENCE: $\alpha = 60^\circ$. — The series of micrographs in Figure 10 show the appearance of evaporated SiO for increasing thickness, seen from above (P1a, P2a, P3a, P5a) and from the side (P1s, P2s, P3s, P5s). These micrographs show a more compact structure than the previous one with very narrow objects oriented in the plane of incidence. Indeed here the width of these objects stay almost constant and we prefer the term *columns* to characterize them. We first observe the side views. For $d_{cal} = 40$ Å (P1s) the *columns* are very small and their tilt is not really measurable. For $d_{cal} = 100$ Å (P2s), the tilt is more visible with a value

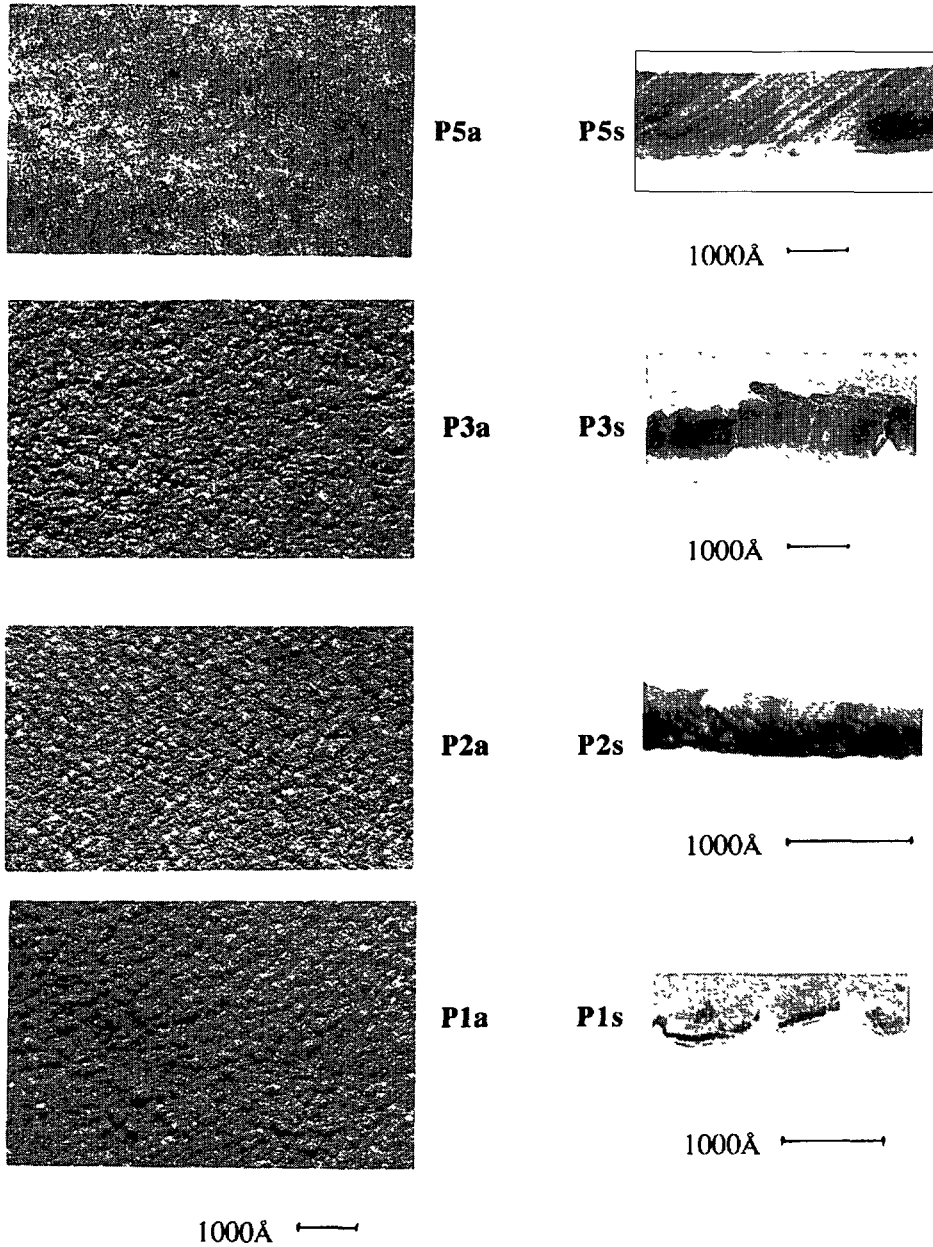


Fig. 10. — Micrographs of SiO films deposited at an angle of incidence $\alpha = 60^\circ$ for different thicknesses (P1 : $d_{cal} = 40 \text{ \AA}$; P2 : $d_{cal} = 100 \text{ \AA}$; P3 : $d_{cal} = 300 \text{ \AA}$; P4 : $d_{cal} = 600 \text{ \AA}$).; seen from the side (right) and from the above (left). The micrographs are presented like in Figure 5. The structure is quite smooth for thin thicknesses (P1, P2) and becomes fully compact for the thicker one (P5).

Table II. — Geometrical parameters of SiO layers with different thicknesses. The layers are evaporated following an angle of 60° and they give a planar nematic liquid crystal orientation. The parameter definitions are the same as for the Table I.

| Plate | $d_{\text{cal}}/\text{\AA}$ | $d_{\text{mes}}/\text{\AA}$ | $l/\text{\AA}$ | $b/\text{\AA}$ | $d_1/\text{\AA}$ | $d_2/\text{\AA}$ | a |
|-------|-----------------------------|-----------------------------|----------------|----------------|------------------|------------------|------------|
| P1 | 40 | 110 | 140 | 40 | 70 | 50 | - |
| P2 | 100 | 310 | 410 | 70 | 110 | 100 | 41° |
| P3 | 300 | 670 | - | 110 | 110 | 110 | - |
| P4 | 600 | 1070 | 1360 | 140-150 | 120 | 150 | 38° |
| P5 | 1500 | 1660 | 2590 | 230 | 235 | 230 | 50° |

of 40° . For $d_{\text{cal}} = 300 \text{ \AA}$ (P3s), the tilt is not visible on this cross section. For $d_{\text{cal}} = 600 \text{ \AA}$, the *columns* show a dense packing with a 50° tilt. For $d_{\text{cal}} = 1500 \text{ \AA}$ (P5s), the tilt is 50° ; at the beginning of their growth, one observes a thin perturbed region which could correspond to a different initial tilt, as also observed in Figure 5, O4s. The *columns* lengths l and their diameters b increase with the calculated thicknesses d_{cal} . The measured thicknesses d_{mes} also increases with d_{cal} , but is closer to d_{cal} than in the grazing incidence case $\alpha = 84^\circ$. The curve $d_{\text{mes}} = f(d_{\text{cal}})$ (Fig. 6) joins the linear dependence $d_{\text{mes}} = d_{\text{cal}}$ for large thickness $d_{\text{cal}} = 1500 \text{ \AA}$. The structure tends to become compact. The geometrical surface mean parameters are listed in Table II. For thin layers the spacing between *columns* d_1 and d_2 are comparable and are lower than in the previous case. Their values seem to increase with d_{cal} but cannot be measured for large d_{cal} . Those values and the diameters b plotted in Table II indicate that in thick layers the *columns* form clusters.

We can characterize the porosity of the SiO film deposited at this angle of incidence, by the ratio $1 - x = 1 - d_{\text{cal}}/d_{\text{mes}}$. We have plotted the variation of this porosity *versus* d_{cal} in Figure 8 and of the averaged diameter b of the *columns* *versus* d_{cal} in Figure 9. The porosity does not vary monotonously. It slightly increases for thin film and then decreases quickly toward zero for thicknesses higher than 100 \AA . The high porosity at 100 \AA is confirmed by P2s where the platinum decorate not only the top but also the back of the *columns*. This difference in porosity between the thin films and the thicker ones is visible on P5s in Figure 10 where we observe a thin perturbed region in the bottom of the film. For the thick films, the decrease of the porosity *versus* d_{cal} corresponds to the increase of b which varies as the square root of d_{cal} .

As it can be seen, the *columns* are very narrow and the porosity is much weaker in this lower incidence case ($\alpha = 60^\circ$) than in the grazing one ($\alpha = 84^\circ$). For thick layers, the porosity tends towards zero but the micrographs show a remaining tilted columnar structure (Fig. 10, P5s).

If we observe the top of the SiO films, their surfaces (micrographs Pa) present small grains of size $\sim 40\text{-}50 \text{ \AA}$ and larger wave length irregularities constituted by the top of the *columns*. In the direction perpendicular to the evaporation plane (d_2), the *columns* come together as visible in Figure 10 (P1a, P2a, P3a). The corresponding oscillation amplitude in this d_2 direction vanishes and its period is multiplied by the number of *columns* which come together. In the evaporation plane, the columnar merging is less visible; it stay an undulation of period d_1 . Its amplitude can be estimated in P2s and P3s as $d_1/10$.

3.3. INTERMEDIATE SITUATION $\alpha = 74^\circ$. — The series of micrographs of Figure 11 shows the appearance of evaporated SiO layers, seen from above (T1a, T2a, T3a) and from the side (T1s, T2s, T3s), for increasing thicknesses. The *columns* structure is also present in this intermediate

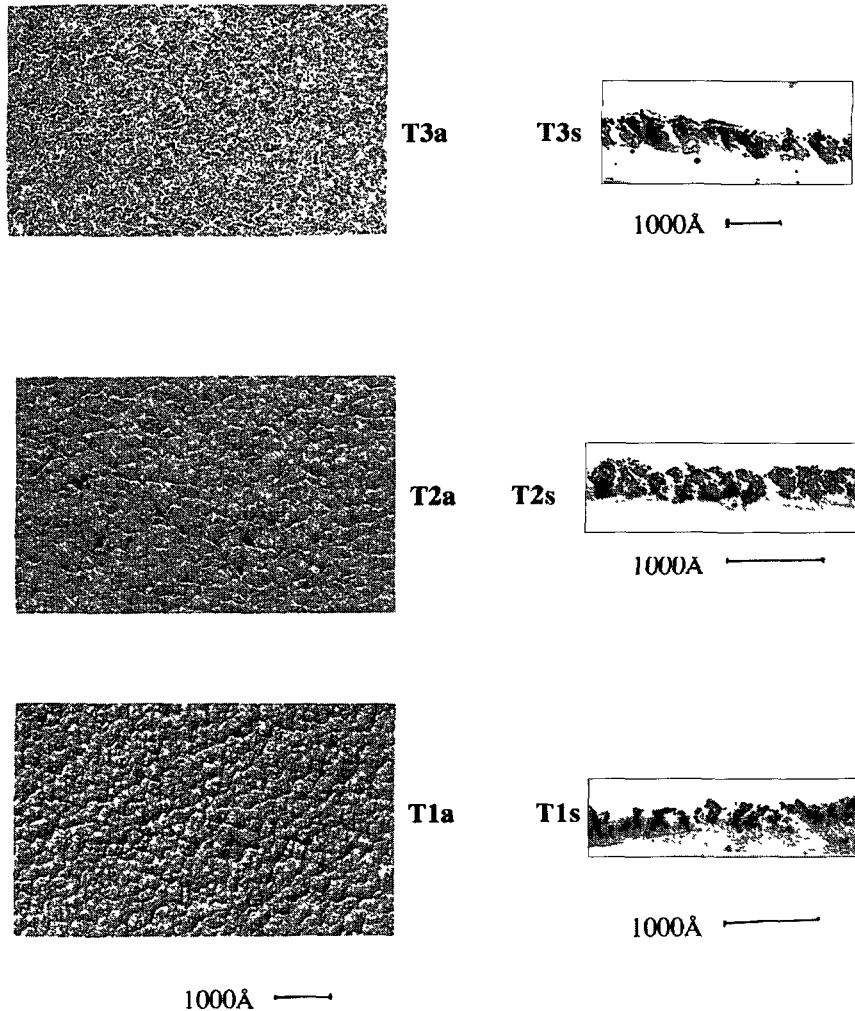


Fig. 11. — Micrographs of SiO films deposited at an intermediate value $\alpha = 74^\circ$ for different thicknesses (T1 : $d_{\text{cal}} = 40 \text{ \AA}$; T2 : $d_{\text{cal}} = 100 \text{ \AA}$; T3 : $d_{\text{cal}} = 300 \text{ \AA}$). Some crevices appear, more visible in T2.

case with an angle of 45° visible on T3s. These *columns* join together in the d_2 direction as clear in T2a. They are separated by deep crevices perpendicular to the evaporation plane, visible on micrographs T1a and T2a (Fig. 11). On the thick film T3, the crevices remain as shown on the view from the side T3s. They are hidden in the view from above because of the *columns* tilt. For very thin layers, the *columns* are less visible than for the other evaporation angles.

Our measured values of the geometrical surface parameters are listed in Table III. The length l and the diameter b of the *columns* increase with d_{cal} (Fig. 9); b is the same as in the case of the grazing incidence evaporation. The spacing between the *columns* remains two times larger in the evaporation plane than in the perpendicular direction. Their values are intermediate between the two previous cases but they do not vary much with the thickness for thin layer. In this case the *columns* grow independently on the substrate without clustering.

Table III. — Geometrical parameters of SiO layers with different thicknesses. The layers are evaporated following an angle of 74° and they give a tilted monostable or bistable nematic liquid crystal orientation. The parameter definitions are the same as for the Table I.

| Plate | $d_{\text{cal}}/\text{\AA}$ | $d_{\text{mes}}/\text{\AA}$ | $l/\text{\AA}$ | $b/\text{\AA}$ | $d_1/\text{\AA}$ | $d_2/\text{\AA}$ | a |
|-------|-----------------------------|-----------------------------|----------------|----------------|------------------|------------------|------------|
| T1 | 40 | 160 | 230 | 110 | 260-300 | 100-150 | - |
| T2 | 100 | 260 | 410 | 150 | 200-300 | 100-150 | 45° |
| T3 | 300 | 580 | 820 | 220 | 270-290 | 100-150 | 45° |

The porosity *versus* d_{cal} is shown in Figure 8. The film is less porous than for the grazing incidence but the behavior of the porosity is similar and seems to saturate around 0.5 for thick films. The crevices volume tends to compare to the *columns* volume. This confirm a mean crevice width comparable to the mean column diameter.

We observe small grains of size 40\AA and large wave length tip of *columns* oscillations at wave length d_1 and d_2 but with very low amplitudes. The *columns* are separated by deep crevices as visible on the side view; their depth is the film thickness and their width is $d_1/2$. They undulate in the d_2 direction following the *columns* with the wave length d_2 and an amplitude close to $d_1/4$.

3.4. EVOLUTION OF THE SiO TOPOGRAPHY AT CONSTANT THICKNESS. — In the previous paragraphs we have studied the evolution of the SiO layers topography *versus* the thickness for three different evaporation angles α . In Figures 5, 11 and 10, we can see the influence of the evaporation angle α for a given thickness. On plates P1, T1 and O1 the layer is thin: $d_{\text{cal}} = 40 \text{\AA}$. On the view from above the increase of the *columns* dimensions *versus* α is visible. For $\alpha = 60^\circ$ (Fig. 10, P1a) and $\alpha = 74^\circ$ (Fig. 11, T1a), the *columns* structure is difficult to see from the top, but for $\alpha = 84^\circ$ (Fig. 5, O1a), the *columns* look big and separated. On the cross section picture the *columns* are visible for $\alpha = 74^\circ$ (Fig. 12, T1s) and $\alpha = 84^\circ$ (Fig. 5, O1s) with a large spacing difference. Plates P2, T2 and O2 have a layer thickness $d_{\text{cal}} = 100 \text{\AA}$. For $\alpha = 60^\circ$ (Fig. 10, P2), one observes compact *columns*. These *columns* become *needles* for $\alpha = 74^\circ$ (Fig. 11, T2), very well-separated for $\alpha = 84^\circ$ (Fig. 5, O2).

3.5. SUMMARY. — Summarizing our observations, we conclude that the SiO obliquely deposited films all present a quasi periodic structure of *columns* or *needles*. For thick films, the *columns* are tilted of about 40° to 50° from the normal of the substrate and oriented toward the evaporation direction. For thin films, the tilt is less observable with a value of 35° . The *columns* diameter (Fig. 9) increases slowly with the layer thickness following about a cube root law. We can remark that the values are the same for the two larger evaporation angles even if, in the case of the grazing incidence, the *needles* remain very far apart.

The SiO film porosity (Fig. 8) decreases with d_{cal} . For $\alpha = 60^\circ$ and $d_{\text{cal}} = 1500 \text{\AA}$, the SiO columnar texture becomes fully compact although for $\alpha = 84^\circ$ and at all thicknesses, the SiO *needles* remain well-separated. For $\alpha = 74^\circ$ and $d_{\text{cal}} = 100 \text{\AA}$, the *columns* join together in the direction perpendicular to the evaporation plane and stay separated by deep crevices in the evaporation plane.

The SiO film roughness increases with the porosity: for the grazing incidence $\alpha = 84^\circ$, the SiO surface is very rough, including irregularities at all spatial periods from 100 to 500\AA ; for $\alpha = 60^\circ$, the SiO films surface appears smoother for all thicknesses, showing low amplitude 200\AA to 300\AA wave length modes. For the intermediate situation ($\alpha = 74^\circ$), the films show

a structure in between the two previous situations, with the increase of the amplitude of the modes corresponding to the crevice and the crevice undulation.

4. Discussion

The topography of SiO films deposited at an angle of incidence on various substrates has been investigated by different EM techniques [6–13]. It is interesting to compare our results with literature data. The more complete study is the work of Goodman *et al.* [10]. Using rotations of the SiO substrate in the transmission electron microscopy, they have studied SiO films with normal thickness between 300 Å and 3200 Å deposited at grazing incidence ($\alpha = 83^\circ$) on a thin amorphous carbon layer. These thicknesses correspond to d_{cal} between 36 Å and 390 Å, very comparable to ours. These films present a semi-periodic structure of separated *columns* (*i.e.*, *needles*) oriented in the plane of incidence and tilted of about 50° from the normal to the substrate. The width of individual *needles* (100 Å–200 Å) and the spacing between themselves (300 Å–600 Å) do not have a great variation with thickness. For an angle of incidence $\alpha = 60^\circ$, the SiO films show a columnar structure for films thickness d_{cal} in between 38 Å and 265 Å. The *columns* angle of inclination is about 30 to 35° from the normal of the substrate. The *column* periodicity is about 80 to 100 Å.

In our present work, we have also observed the *needles* to *columns* transition between the incidence $\alpha = 84^\circ$ and $\alpha = 60^\circ$. Our tilt angles are a little bit different from reference [10]: they stabilize for both thick *needles* and *columns* to 40° – 50° . Only for thin layers we do find a 35° tilt. Taking into account the difference between our geometry, our *needles* diameter and spacing compare reasonably, but we do observe a regular increase of diameter with thickness, accompanying the period doubling in the evaporation plane. Our constant transverse period is a new information. The one difference between our two works is the nature of the substrate, amorphous carbon film for reference [10] and ITO on glass for us. This could explain the different behavior of thin SiO films.

Later and using scanning electron microscopy and transmission electron microscopy observations with a cleavage technique, van Sprang *et al.* [13] show this columnar structure in SiO layers with real thickness of 500 Å deposited at oblique incidence. The *columns* are found tilted in the evaporation plane with an angle of about 22° independent of the evaporation angle. This tilt angle seems for us surprisingly small. On the cleavage micrograph of Figure 4b in reference [13], one do observe an apparent *columns* tilt angle of 45° in a cleavage plane also tilted of 45° : this corresponds to a real columnar tilt of 35° (and not 22°), closer to our measurement.

The other works quoted in references present less complete data but in agreement with ours. Reference [12] for instance gives a single cross section of a SiO film grown at $\alpha = 85^\circ$ incidence. The *columns* tilt goes from an initial value of 30° toward 50° in good agreement with our present finding. No data of surface roughness were explicitly given in these previous works.

5. Nematic Alignment and Correlation with SiO Topography

5.1. NEMATIC ORIENTATION. — For the plates P1, P2, P3, P4, P5, we find a planar orientation ($\theta = 90^\circ$, $\varphi = 90^\circ$), perpendicular to the evaporation plane. For the O plates, we find an oblique orientation inside the evaporation plane ($\varphi = 0^\circ$) with various tilts: O1: $\theta = 70^\circ$, O2 : $\theta = 65^\circ$, O3 : $\theta = 58^\circ$, O4 : $\theta = 55^\circ$. This last value corresponds to the “magic angle” $\theta_m \equiv 55^\circ$ ($\cos \theta_m = (1/\sqrt{3})$) which is chosen by the 5CB nematic on a melted surface (15, 28, 29). For the intermediate plates, we find an intermediate

orientation: T1 shows a bistable anchoring with $\theta = 70^\circ$, $\varphi = \pm 35^\circ$; for T2 and T3, we find an oblique anchoring with tilt in the evaporation plane $\varphi = 0^\circ$, $\theta = 67^\circ$ and 64° respectively.

The results of the nematic orientation confirm the ones already obtained in the reference [14].

5.2. CORRELATION WITH SiO TOPOGRAPHY. — If we compare in Figure 8 the porosity of P1, T1 and O1, we can guess that the porosity is the origin of the transition between the planar orientation on P1 to the oblique orientation on O1 toward the bistable orientation on T1. The observation of the porosity of P2, T2, O2 and P3, T3, O3 do not confirm this hypothesis: T2, T3, O2, O3 give the oblique orientation even if the porosity of T2 and T3 is lower than the one of P2 and P3. The shape of the void seems to be more important than the porosity: well-separated *needles* and crevices give nematic oblique orientation; closely packed *columns* give planar orientation.

5.3. COMPARISON WITH PREVIOUS MODELS

5.3.1. *The Theoretical Models.* — In the first model of Berreman [20] and de Gennes [1], a soft surface undulation (small wave vector \mathbf{q} , small amplitude A) can induce a nematic planar orientation with director \mathbf{n} perpendicular to \mathbf{q} , to escape surface curvature. It was later predicted by Barbero *et al.* [21] that a rapid surface undulation or a surface roughness could induce such a high curvature that the nematic surface order parameter S would decrease and even become zero *i.e.*, the nematic phase would melt. The melting should occur when $Aq^2\xi \geq 1$, where ξ is the coherence length associated with the nematic-isotropic transition. We can deduce from this model that if the roughness of the surface is anisotropic, the melting parameter is not the same in the different directions. To minimize the surface energy the nematic would choose the azimuthal orientation which minimize the melting energy and not the elastic one. In this case the azimuthal nematic orientation onto the surface may be given by a minimum melting condition. On the other hand, as indicated by Barbero *et al.* [15], this order parameter variation creates an order-electricity polarization near the surface which tends to orient the molecules on the surface toward the magic angle θ_m . The competition between the van der Waals interaction with the surface and this order-electric effect may give the zenithal molecular orientation. That gives a new model for the orientation on rough surfaces: the ordoelectrical and partial melting orientation.

5.3.2. *The Values of the Melting Parameter.* — To compare the models and our experimental results we list in Table IV the values of the melting parameter: $Aq^2\xi$ for the studied plates. We first present general remarks about the determination of the coherence length, ξ , the amplitude and the wave vector of the surface roughness, A and q .

In the Table IV we estimate ξ , as 20 \AA . ξ has been measured in the isotropic phase as $\xi_{0I} \approx 5 \text{ \AA}$ [22–24]. An extrapolation in the nematic phase gives $\xi_{0n} \approx \xi_{0I}/\sqrt{2} \approx 3.5 \text{ \AA}$. At room temperature, 10 degrees lower than the nematic transition temperature T_c , using the Landau-de Gennes theory, we estimate ξ as $\xi_0 \times (300/10)^{0.5} \approx 20 \text{ \AA}$. The corresponding wave length: $\lambda_c = 2\pi\xi$ is in the range of 120 \AA .

In Table IV, q and A are obtained by looking at the large wave vector distortions: the columnar tip modes, the crevices modes and the *needles* modes. The spatial period λ of these modes is of the order of d_1 and d_2 , the distances between the *columns* or *needles* along the evaporation plane and perpendicular to it. The corresponding amplitude A are estimated from the cross sections.

The important and obvious conclusion we can make with the values of the melting parameter listed in Table IV is that for every plate there is at least one direction where the Berreman

Table IV. — Values of the melting parameter $Aq^2\xi$ calculated for the different plates and different orientations of the molecules. $A_1q_1^2\xi$ are the values if the molecules are oriented parallel to the evaporation plane ($q_1 = 2\pi/d_1$), $A_2q_2^2\xi$ if they are perpendicular to it and on the top of the layer and $A_3q_3^2\xi$ if they are inside the crevices.

| Plate | $d_{mes}/\text{\AA}$ | $d_1/\text{\AA}$ | $A_1/\text{\AA}$ | $A_1q_1^2\xi$ | $d_2/\text{\AA}$ | $A_2/\text{\AA}$ | $A_2q_2^2\xi$ | $A_3/\text{\AA}$ | $A_3q_3^2\xi$ |
|-------|----------------------|------------------|------------------|---------------|------------------|------------------|---------------|------------------|---------------|
| P1 | 110 | 70 | - | | 50 | - | - | | |
| P2 | 310 | 110 | 25 | 1.6 | 100 | \ll | $\ll 1$ | | |
| P3 | 670 | 110 | 25 | 1.6 | 110 | \ll | $\ll 1$ | | |
| P4 | 1070 | 120 | 30 | 1.6 | 150 | \ll | $\ll 1$ | | |
| P5 | 1660 | 235 | 70 | 1 | 230 | \ll | $\ll 1$ | | |
| O1 | 330 | 350 | 165 | 1 | 230 | 165 | 2.4 | | |
| O2 | 710 | 650 | 355 | 0.7 | 200 | 355 | 7 | | |
| O3 | 1370 | 810 | 680 | 0.8 | 300 | 680 | 6 | | |
| O4 | 2370 | 800 | 1180 | 1.5 | 300 | 1180 | 12 | | |
| T1 | 160 | 280 | 80 | 0.8 | 125 | \ll | $\ll 1$ | 30 | 1.5 |
| T2 | 260 | 250 | 130 | 1.6 | 125 | \ll | $\ll 1$ | 40 | 2 |
| T3 | 580 | 280 | 290 | 3 | 125 | \ll | $\ll 1$ | 55 | 2.8 |

hypothesis of a soft surface undulation does not apply. We have then to take the melting into account. We make now a more detailed analysis of these data.

5.3.3. *The Partial Melting on the Different Plates.* — For the P plates (P2, P3, P4 and P5), the amplitudes A_1 of the surface undulation in the d_1 direction listed in the Table IV are measured on the cross sections. In the d_2 direction, even if small undulations are visible on the view from above, the observed merging of the *columns* induces us to postulate a smaller amplitude ($A_2 \ll A_1$). It results in $A_2q_2^2\xi \ll A_1q_1^2\xi \approx 1$. To escape a surface melting along d_1 ($A_1q_1^2\xi \approx 1$), the nematic has to take a planar orientation along d_2 ($A_2q_2^2\xi \ll 1$) with molecules laying perpendicular to the evaporation plane ($\varphi = 90^\circ$, $\theta = 90^\circ$). This explains well the observed planar orientation of the nematic onto the P plates.

For the O plates, the *needles* are separated in the d_1 and d_2 directions. The amplitudes of the corresponding undulation modes are $A_1 \approx A_2 \approx d_{mes}/2$. In Table IV the obtained $A_2q_2^2\xi$ values are larger than the $A_1q_1^2\xi$ ones that are close to 1. This suggests that the molecules should align in the evaporation plane along the d_1 direction to lower the surface melting. However even in this direction the surface melting may occur and the ordo-electric effect should be brought into play, it gives the observed tilted orientation. If we consider the *needles* lateral area, we can observe local irregularities of period 100 Å to 150 Å on it as clearly visible in Figure 5 (O3a). These irregularities are not taken into account if we only consider the undulations in the d_1 direction and the d_2 one, but they can also induce a nematic surface order melting in between the *needles* and should help the mean surface melting. The total melting has been recently observed by plasmon resonance for the thickest SiO layer (O4) in between the *needles* and on their top for an other nematic compound (MBBA) [26]. This confirms our hypothesis of surface melting. The molecular orientation onto the O plates in the evaporation plane corresponds well to the choose of a minimum of the surface melting.

For the T plates the undulation amplitude in the d_1 direction is $A_1 \approx d_{mes}/2$ as visible

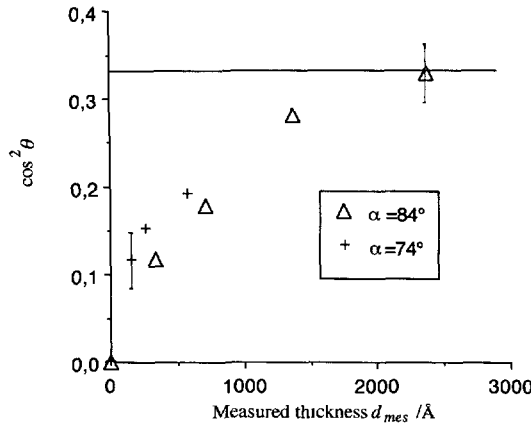


Fig. 12. — Values of the surface molecular tilt angle cosine *versus* the SiO film thickness. For thick layers, the curves tend to saturate close to $\cos^2 \theta = 1/3$ (shown by the line), as predicted in the case of strong ordoelectric effect.

in Figure 11 (T1s, T2s and T3s). In the d_2 direction, when the film thickness increases, the progressive *columns* merging suppress the undulation. It stays a visible smaller undulation in T1a that practically disappears in T2a and probably in T3a where the large thickness blurs the image. The corresponding $A_1 q_1^2 \xi$ and $A_3 q_2^2 \xi$ values are in Table IV. If, for these T plates, we use the same melting criterion as for the P and O plates we will say that the nematic would align in the planar orientation along the d_2 direction ($\varphi = 90^\circ$) as for the P plates. This is not what we observe onto these T plates. To explain this, we propose to consider not only the undulation on the column's top but also the effect of the crevices. Indeed the liquid crystal molecules may penetrate in the crevices. Inside them, the undulations on their lateral surfaces have a period d_2 and an amplitude A_3 visible on the top views and close to the column's diameter divided by 4. The values of $A_3 q_2^2 \xi$ in Table IV indicate a melting in the crevices for the planar orientation in the d_2 direction; it explains a repulsion from that direction increasing with the depth of the crevice, d_{mes} . This repulsion and the ordo-electric attraction toward the magic angle explain the bistable oblique orientation observed onto the T1 plate and the monostable oblique orientation in the evaporation plane onto the T2 plate and the T3 plate.

5.3.4. *The Zenithal Orientation.* — The molecular tilt angle of the molecules onto the surface is presented in Figure 12. We plot $\cos^2 \theta$ *versus* the measured thickness of the SiO layer, d_{mes} , for the two evaporation angles: $\alpha = 74^\circ$ and $\alpha = 84^\circ$. When the thickness increases, $\cos^2 \theta$ goes from 0, the planar orientation without SiO, to $1/3$, the magic angle obtained for thick rough layer. This indicates that when the rough layer thickness increases, the ordo-electric effect increases compared to the van der Waals interaction with the substrate that induces planar orientation. The obtained magic angle confirms that the nematic melts close to the rough surface.

5.3.5. *Conclusion of the Comparison.* — The simple Berreman-de Gennes model taking into account only the elastic energy from the surface undulation cannot explain the azimuthal and zenithal orientation onto the three kinds of surface. The surface melting is proved in one case by the Papanec measurements [25]. We have in this work an indirect evidence of the surface partial melting from the values of the melting parameter listed in Table IV. The new model of orientation by ordo-electricity and along the direction that minimize the partial melting on

the surface explain well the different observed orientations. We have here an experimental confirmation of this model.

Note however that the predictions of the two models, the elastic Berreman-de Gennes and the partial melting one, are almost the same for the azimuthal orientation: the molecules on the surface tend to orient along the direction of minimum of curvature. The main difference appears for the value of the anchoring energy. The elastic model gives an azimuthal anchoring energy by unit area that diverges for high q : $W_s = KA^2q^3/4$. For the studied surface this energy could reach 30 erg/cm^2 . This corresponds to an unphysical surface extrapolation length $\approx 3 \text{ \AA}$. The new model, in the limit of high roughness, gives a surface energy: $W_s \approx K_s/\xi_s$ where K_s is the elastic curvature constant close to the rough surface and ξ_s is the coherence length of the nematic-isotropic transition near the rough surface. W_s is then proportional to the cube of the order parameter near the surface and goes to zero for complete melting induced by the surface. The typical order of magnitude for the azimuthal surface energy: $W_s \approx 0.01 \text{ erg/cm}^2$ [27] corresponds to a partial melting with the surface order parameter close to one fifth of the bulk order parameter.

6. Conclusion

To explain the observed transition of the orientation of a nematic liquid crystal onto a SiO layer, we have studied the topography of this layer by transmission electron microscopy. We have analyzed the surface anchoring transitions, using various models.

Our electron microscopic observations have been made in two geometries: normal to the layer and on cross sections obtained by ultramicrotomy. We have varied the evaporation angle from 60° to 84° and the SiO thickness from 40 \AA to 1500 \AA .

- For all the studied evaporation conditions the SiO layer is made of individual *columns* or *needles* tilted in the plane of evaporation. Their tilt angle from the normal of the substrate is about 45° for large enough SiO thicknesses. For very thin layer only ($d \approx 40 \text{ \AA}$), we observe a tilt of 35° probably due to a substrate interaction.
- When the layer thickness increases from 100 \AA to 1500 \AA , the diameter of *columns* or *needles* increases but saturates close to 250 \AA for the three evaporation angles.
- When the evaporation angle α , goes from a grazing incidence ($\alpha = 84^\circ$) to a tilted one ($\alpha = 60^\circ$), we observe a transition between well-separated *needles* to packed *columns*. Between these two cases the *columns* joint together in the direction perpendicular to the evaporation plane making walls separated by deep crevices.

Looking at the nematic liquid crystal surface orientation on these plates, we find that the transition of the nematic orientation on the SiO film from planar to tilted corresponds to the film texture transition from packed *columns* to separated *needles*. The intermediate crevice texture gives the bistable anchoring for thin films (wall height $\approx 150 \text{ \AA}$) and tilted anchoring when the film is thicker (wall height $> 300 \text{ \AA}$).

All our observations indicate that the roughness of the SiO films is very important. The Berreman-de Gennes model cannot be used to explain the orientation mechanism onto the SiO films. This elastic model works only on smoother surfaces. We have measured the amplitudes and the wave lengths of the roughness. We observe at least one direction on the surface along which the molecules cannot orient without partial melting.

Our electron microscopic study of the SiO films proves the validity of the new model of surface orientation of the nematic liquid crystal by partial melting and ordo-electric effect.

The zenithal orientation is given by the attraction on the magic angle cone due to the ordoelectric effect and the van der Waals interaction with the anisotropic surface. The azimuthal orientation is along the direction of minimum roughness to minimize the order parameter decrease (partial melting) on the surface. The azimuthal anchoring energy is mainly given by the difference of surface energy between the partial melting in the different directions; this energy vanishes in the case of complete melting.

Acknowledgments

We are very indebted to Dr. T. Gulik who introduced us to the delicate electron microscopy techniques and allowed us to work in his laboratory. We thank M. Boix for SiO deposition.

References

- [1] See for instance de Gennes P.G., *The Physics of Liquid Crystals* (Clarendon Press, Oxford, 1974).
- [2] A review on this subject is: Cognard J., *Mol. Cryst. Liq. Cryst. Suppl. Ser. A* **5** (1982) 1; Jerome B., *Rep. Prog. Phys.* **54** (1991) 391.
- [3] Janning J.L., *Appl. Phys. Lett.* **21** (1972) 173.
- [4] Guyon E., Pieranski P. and Boix M., *Appl. Eng. Sci. Lett.* **1** (1973) 19.
- [5] Urbach W., Boix M. and Guyon E., *Appl. Phys. Lett.* **25** (1974) 19.
- [6] Priest J., Caswell H.L. and Budo Y., *J. Appl. Phys.* **34** (1963) 347.
- [7] Dixon G.D., Brody T.P. and Hester W.A., *Appl. Phys. Lett.* **24** (1974) 47.
- [8] Pollack J.M., Haas W.E. and Adams J.E., Abstract of 6th Intern. Liquid Crystal Conf., Kent State Univ., Kent OH and August 23-27 (1976).
- [9] Yamashita M. and Yoshifumi Y., *Appl. Phys.* **15** (1976) 11.
- [10] Goodman L.A., Meginn J.T., Anderson C.H. and Digeronimo F., *IEEE Trans. Electron. Devices* **24** (1977) 795.
- [11] Cheng J., Boyd G.D. and Storz F.G., *Appl. Phys. Lett.* **37** (1980) 716.
- [12] Armitage D., *J. Appl. Phys.* **51** (1980) 2552.
- [13] van Sprang H.A. and Aartsen R.G., *J. Appl. Phys.* **56** (1984) 251.
- [14] Monkade M., Boix M. and Durand G., *Europhys. Lett.* **5** (1988) 697.
- [15] Barbero G., Dozov I., Paliarne J.F. and Durand G., *Phys. Rev. Lett.* **56** (1986) 2056.
- [16] Barberi R. and Durand G., *Phys. Rev. A* **41** (1990) 2207.
- [17] Reimer L., *Transmission Electron Microscopy* (Springler Verlag, Berlin, 1993).
- [18] Resine Mecapressc from PRESI (Grenoble France).
- [19] Karat P. and Madhusudana N.V., *Mol. Cryst. Liq. Cryst.* **36** (1976) 51.
- [20] Berreman D.W., *Phys. Rev. Lett.* **28**, (1972) 1683.
- [21] Barbero G. and Durand G., *J. Phys. II France* **1** (1991) 651.
- [22] Leadbetter A.J., Richardson R.M. and Colling C.N., *J. Phys. Colloq. France* **36** (1975)
- [23] van Sprang H.A. *J. Phys. France* **44** (1983) 421.
- [24] Hsiung H., Rasing T. and Shen Y.R., *Phys. Rev. Lett.* **57** (1986) 3065.
- [25] Crawford G.P., Ondris-Crawford R.J., Doane J.W. and Zumer S., *Phys. Rev. E* **53** (1996) 3647.
- [26] Papanec J. and Martinot-Lagarde Ph., *J. Phys. II France* **6** (1996) 205.
- [27] Nobili M., Durand G., *Europhys. Lett.* **25** (1994) 527.
- [28] Faetti S. and Palleschi V., *Phys. Rev. Lett.* **30** (1984) 3241.
- [29] Faetti S. and Palleschi V., *J. Phys. France Lett.* **45** (1984) 313.